International Journal of Environmental Sciences
ISSN: 2229-7359
Vol. 11 No. 10s, 2025
https://www.theaspd.com/ijes.php

The low temperature catalytic decomposition of gaseous ozone on Nano Manganese dioxides and the effect of phase structure

Mohan Kurra[1], Shireesha Boyapati[1*], Swetha Gujarathi[2]
[1]Department of Pharmaceutical Chemistry, Telangana University, Nizamabad-503322, India.
[2]Department of Chemistry, RGUKT Basar, Mudhole-504107

Abstract
Four nano manganese dioxides with different phase structures (α-, β-, γ-, and δ-MnO_2) were prepared by hydrothermal method and characterized by X-ray powder diffraction, surface area, H_2-temperature programmed reduction, scanning electron microscopy, and X-ray photoelectron spectroscopy. The prepared catalysts were tested for ozone decomposition and found considerable activity difference, which was due to their change in the MnO_2 phase structure. The γ-MnO_2 showed 100 % ozone decomposition among the four catalysts, while α-, β-, and δ-MnO_2 catalysts exhibited 92, 70, 35 %, respectively after 480 min. The characterization results suggested that the decomposition of ozone is primarily dominated by the tunnel structure, surface oxygen vacancies and average oxidation state (AOS) of Mn rather than specific surface area and reducibility. However, the random tunnel structure of γ-MnO_2 has provided most active surface oxygen vacancies and the lowest AOS of Mn on the catalyst surface. Therefore, the γ-MnO_2 catalyst presented the highest ozone decomposition capacity among the other MnO_2 catalysts. Due to this, γ-MnO_2 may potentially be used as a catalyst in the purification of ozone contains waste gases as well as in the application of ozone assisted catalytic oxidation of volatile organic compounds.
Keywords: *MnO_2; Phase structure; ozone decomposition; oxygen vacancy; Morphology.*

1. INTRODUCTION

All we know, ozone layer at stratosphere is protecting the life on earth from the ultraviolet radiations. But the ozone is highly toxic and it acts as a pollutant if it is at ground level (troposphere) because of its strong oxidizing ability and odor[1]. According to the Environmental Protection Agency (EPA) regulations, prolonged exposure of ozone in terms of 8 h average concentration of 0.075 ppm causes savior health problems such as respiratory illness, headache and reduced immune system function[2]. Hence, the decomposition of ozone at ground level is an important task from the health and environmental point of view[3]. The main sources for the ground level ozone are photocopiers, laser printers, and the residual ozone from the processes such as sterilization, deodorization, waste water treatment, ozone catalytic oxidation of VOCs[4-6].

There are several methods such as thermal decomposition, adsorption and catalytic decomposition have been reported[7,8], but the catalytic decomposition proved to be a promising method for the decomposition of ozone because of its low operating temperature at low/room temperatures[9]. Dhandapani and Oyama summarized previous studies and reported that the metal oxide showed better catalytic activity than that of respective metals and also reported that the manganese oxides (alumina supported) exhibited the better catalytic activity among the other metal oxides for the ozone decomposition[5]. The high ozone decomposition capacity over manganese oxides was attributed to its changeable valance, morphology and oxygen vacancies[10-14]. Along with supported manganese oxides, the unsupported manganese oxides also proved its ability for high ozone decomposition[15-17]. Tang et al., reported that the higher oxidation state facilitated the high ozone decomposition over manganese oxides[18].

On the other hand, MnO_2 is proved to be promising candidates among the other transition metal oxides for the catalytic oxidation of VOCs due to its distinctive physical and chemical properties, such as multivalent nature and non-stoichiometric composition[19,20]. In recent years, most of the studies have been focused on the relationship between the morphology, phase structure and catalytic activity of MnO_2 catalysts[21-23]. Liang et al.,

synthesized different MnO_2 phase structures (α-, β-, γ- and δ-MnO_2) with the same morphology (nanorods) and employed for the CO oxidation[24]. The results showed that the crystal phase and the tunnel structure of the catalysts played a main role in the activities for CO oxidation. In the similar way, Si et al., prepared various MnO_2 phase structures and examined the phase structure and activity relationship for the oxidation of toluene. The γ-MnO_2-SR structure possessed the best activity among the other samples, which was due to the three-dimensional macroporous and mesoporous morphology[25]. Very recently, Wang et al., reported the ozone decomposition over cryptomelane (α-MnO_2) type phase structure and showed 80 % conversion at 30°C[10]. Whereas, Jia et al., reported ozone decomposition over α, β and γ-MnO_2 phase structures and observed the high ozone conversions on α-MnO_2 phase structures. The better activity over α-MnO_2 was attributed to the density of oxygen vacancies on the surface of the catalyst[26].

However, MnO_2 form many kinds of polymorphs, such as α, β, γ, δ and λ-MnO_2, when the MnO_6 octahedral units are linked in different ways[27]. It was mostly accepted that the phase structure can considerably influence the catalytic activity of MnO_2[24]. Hence, it is important to find the variation in the decomposition of ozone over various MnO_2 phase structure. So, the present study focused on the preparation of α-, β-, γ- and δ-MnO_2 phase structures and their performance on the decomposition of ozone at 30 °C.

2. EXPERIMENTAL

2.1. Preparation of catalysts

The four types of manganese oxide with different phase structures prepared by a hydrothermal method according to the previous report[28]. All the reactants mixed in 80 mL distilled water for about 30 min to form a homogeneous solution and further transferred to a Teflon lined stainless steel par reactor (100 mL). After that, the par reactor heated to following temperatures.

For α-MnO_2, 0.525 g $MnSO_4.H_2O$ and 1.25 g $KMnO_4$ reacted at 160 °C for 12 h, for β-MnO_2, 1.69 g $MnSO_4.H_2O$ and 2.28 g $(NH_4)_2S_2O_8$ reacted at 140 °C for 12 h, for γ-MnO_2, 3.375 g $MnSO_4.H_2O$ and 4.575 g $(NH_4)_2S_2O_8$ reacted at 90 °C for 24 h, and for δ-MnO_2, 0.275 g $MnSO_4.H_2O$ and 1.5 g $KMnO_4$ reacted at 240 °C for 24 h. The final products filtered, washed, dried at 80 °C for 12 hours and then calcined at 300 °C in a continuous flow reactor.

2.2 Characterization of catalysts

The above-prepared catalysts were characterized by BET surface area, XRD, SEM, TPR and XPS analysis. The specific surface areas of the catalysts were measured by a multipoint nitrogen adsorption isotherm at -196 °C. The nitrogen adsorption-desorption isotherms were obtained on an M/s. Micromeritics Instruments surface area analyzer. Prior to this, the catalyst (0.1 g) sample was loaded into a quartz reactor and degaussed at 200 °C for 3 h to desorb the moisture.

X-ray diffraction (XRD) patterns of calcined and used forms of the catalysts were recorded on a X-ray diffractometer (M/s. Shimadzu Corporation) using Ni filtered Cu K_α radiation (λ= 1.5406 Å) with a scan speed of 2° per min and a scan range of 10-80° at 30 KV.

The extent of reducibility of catalyst was measured by H_2-temperature programmed reduction (H_2-TPR) on a TPR unit (M/s. Nuchrom Technologies) equipped with a thermal conductivity detector (TCD). The 5.6 % H_2 in argon mixture was passed through a catalyst (0.1 g) at a flow rate of 50 mL/min while increasing the temperature from 40 to 600 °C at a rate of heating 10 °C/min.

The surface morphology of MnO_2 catalysts analyzed with a FEI Quanta 200 scanning electron microscope (SEM). Prior to this, the samples coated on a thin carbon tape to avoid charge effect, and the images recorded at a magnification of 10000.

The surface atom properties were measured at room temperature with an X-ray photoelectron spectroscope (XPS, M/s. Oxford Instruments) with an Al anode for K_α ($h\nu$ = 1486.7 eV) radiation. The binding energy values were calibrated by using the C1s peak (284.8 eV).

2.3. Ozone decomposition experiments

Activity experiments were carried out in a continuous flow, fixed-bed quartz reactor (id of 9 mm) at atmospheric pressure. The 100 mg of catalyst mixed with 300 mg of quartz beads and loaded between two quartz wool plugs in a reactor and mounted vertically in an electrically heated tubular furnace (Carbolite, USA). Prior to the reaction, the catalyst heated at 100 °C in the air flow for 30 min. The standardized ozone generator (Eltech engineers, India) used to generate the ozone by passing the dry oxygen (100 mL/min, 99.9% Alchemie gasses, India) with a precise mass flow controller (Sierra instruments, The Netherlands). The generated ozone was diluted with compressed air (900 mL/min) to maintain the V_{total} of 1000 mL/min. The un-decomposed was ozone analyzed with an ozone analyzer (M/s. Eltech Eng. India, range 0-200 g/m^3) and the residual ozone was scrubbed with KI solution.

3. RESULTS AND DISCUSSION

3.1 XRD studies

From the XRD results (**Figure.1**), the lattice constants of prepared catalysts are in good agreement with the respective phase structures. The XRD pattern of α-MnO_2 is well indexed to a cryptomelane-type manganese oxide (JCPDS 29-1020/44-0141), whereas, the XRD patterns of β-MnO_2 and γ-MnO_2 are in good agreement with pyrolusite-type (JCPDS 24-0735) and nsutite-type (JCPDS 14-0644) manganese oxides, respectively. On the other hand, the XRD pattern of δ-MnO_2 is characteristic of a birnessite-type manganese oxide with a layered structure (JCPDS 80-1098 / 43-1456). The XRD patterns indicate that the prepared catalysts are well crystallized and no impurity phase could be detected. The structural variations of manganese oxides result from the different bonding ways of the basic MnO_6 octahedral units[24].

From the literature, α-, β-, γ-, and δ-MnO_2 structures (**Figure 2**) are all formed by combining the chains of MnO_6 octahedra, which results infinite channels (tunnels) with different dimensions. The ways in which the corners and edges of the MnO_6 octahedral units are combined are important in terms of the tunnel structure; the tunnel size, based on the number of octahedral subunits (n × m), can be used to define different crystallographic forms[24, 29] α-MnO_2 consists of double chains of edge-sharing MnO_6 octahedra, which are linked at corners to form (2 × 2) and (1 × 1) tunnels that extend in a direction parallel to the c-axis of the tetragonal unit cell. The sizes of the (2 × 2) and (1 × 1) tunnels are ~4.6 and ~1.9 Å, respectively[27.] The single chain of β-MnO_2 is linked with the adjacent chains through common corners of the MnO_6 octahedra, resulting in (1 × 1) tunnels[30]. The crystal structure of γ-MnO_2 consists of random intergrowth of ramsdellite ((2 × 1) tunnels, ~2.3 Å) and pyrolusite ((1 × 1) tunnels) structures, with clear stacking faults[29, 31]. In contrast, δ-MnO_2 forms a 2D layer structure and it is theoretically built up from layers of edge sharing MnO_6 octahedra, and the spacing between the layers is ~7 Å [32].

3.2 Surface morphology studies

The surface morphology of synthesized MnO_2 catalysts observed by SEM technique and shown in **Figure.3** (two magnifications for each sample). From the results, α-MnO_2 presents nanorod like structure with a wide range of dimensions; the diameter and length of the nanorods ranged from 50 to 150 nm and 0.5 to 3 μm, respectively. Whereas, β-MnO_2 consist of many fine nanofibers accumulated together to form bowls of several μm in diameter and the diameter and length of the nanofibers ranged from 20 to 100 nm and 0.2 to 1 μm, respectively. On the other hand, γ- and δ-MnO_2 catalysts are shown spherical nanostructures of several μm in diameter. The diameter of spherical nanostructure of γ-MnO_2 is about 3 to 5 μm and it is composed by MnO_2 nanofibers with sharp tips, like an urchin-like cluster and the diameter of these nanofibers are in the range of 5 to 50 nm. Whereas, the δ-MnO_2 spherical morphology is built by many interleaving nanoflakes (like a curling lamellar structure), which are grown from the root of the sphere and the gap between the nanoflakes at the top of the sphere is in the range of 50 to 100 nm. The sizes of the δ-MnO2 spheres are in

the range of 0.3 to 0.8 μm and these spheres are looked to be highly aggregated. Overall, it appears that all the four MnO_2 catalysts are shown nanostructures with various morphologies.

3.3 BET-SA studies

The N_2 adsorption/desorption isotherms and corresponding BJH pore size distributions of MnO_2 catalysts are shown in **Figure.4**. From the results, all the catalysts have type IV isotherms with a type H3 hysteresis loop, indicating a mesoporous structure[19,33]. The α- and δ-MnO_2 catalysts have similar hysteresis loops in the relative pressure (P/P_o) range of 0.5 to 1, whereas β and γ-MnO_2 shows a hysteresis loop at a higher P/P_o range, i.e., 0.9 to 1. The fine hysteresis loops of α, β and γ-MnO_2 could result from inter nanorod and nanofiber spaces, respectively[32,34]. Whereas, the wide hysteresis loop of δ-MnO_2 might be ascribed to the presence of mesoporous interleaved nanoflakes[32]. The insets in **Figure.4** show the BJH pore size distribution of each catalyst. The maximum pore sizes of α-, β-, γ- and δ-MnO_2 catalysts are 3.1, 2.0, 2.6, and 3.8 nm, respectively. From the BET surface area results (**Table 1**.), the δ-MnO_2 possesses higher surface area (164 m^2/g) and pore volume (0.42 cm^3/g) among all other catalysts and the order of surface area and pore volume is β-MnO_2 < γ-MnO_2 < α-MnO_2 < δ-MnO_2. The difference in the surface area and pore volumes is might be due to the difference in the crystal structures and the size of the MnO_2 particles. The lowest surface area of β-MnO_2 could be due to its smallest tunnel size (1 x 1) resulting from the densely packed MnO_6 octahedra[25]. Conversely, the high surface area of α-MnO_2 and δ-MnO_2 might be due to their larger channel crystal dimensions (2 x 2 tunnel and layered) than that of β-MnO_2[25]. The γ-MnO_2 catalyst shown much similar moderate surface area and pore volume, which is related to its moderate tunnel size (2 x 1).

3.4 Reducibility studies

The reducibility of MnO_2 catalysts are investigated by using H_2-TPR experiments and the results displayed in **Figure.5**. From the results, the α and δ-MnO_2 catalysts shown similar H_2 consumption/reduction peaks in the temperature region of 250 to 400 °C and which are very different from the β- and γ-MnO_2. The α and δ-MnO_2 exhibited two overlapped reduction peaks in a narrow temperature range of 300 to 400 °C, with a T_{max} of 372 and 355 °C, respectively, which may be attributed to the reduction of MnO_2 to MnO with Mn_2O_3 and Mn_3O_4 as the intermediates[24,28]. Because, the final green color product, which was observed in the H_2-TPR experiment might be due to the formation of MnO. On the other hand, two distinctive reduction peaks are observed for β and γ-MnO_2 catalysts. The β-MnO_2 catalyst shown a first reduction peak centered at 372 °C, and the second broad peak at 495 °C. The reduction pattern of γ-MnO_2 is similar to β-MnO_2, but the peak position shifted to little higher temperature, shown at 393 and 555 °C, respectively. The lower temperature peak attributed to the reduction of MnO_2 to Mn_3O_4, whereas the higher temperature peak ascribed to the reduction of Mn_3O_4 to MnO[32]. These results indicate that the reducibility of the four catalysts are in the order of γ < β < α < δ-MnO_2.

The amounts of H_2 consumption is calculated and listed in **Table 1**. Theoretically, the consumption of H_2 for the reduction of MnO_2 to Mn_3O_4 and Mn_3O_4 to MnO are 7.67 and 4.37 mmol/g (total 12.04 mmol/g), respectively[26,35]. From the results, all the MnO_2 catalysts exhibited more or less equal values to the theoretical. The α and δ-MnO_2 catalysts shown less values / consumed less H_2 than the β and γ-MnO_2 catalysts, which may resulted from the presence of interstitial cations (K^+) and water in their structures[26]. These results are in line with the reported results.

3.5 ozone decomposition studies

The decomposition of ozone as function of time studied over α-, β-, γ- and δ-MnO_2 catalysts at a GHSV of 600000 $mL/g_{cat}.h$, temperature of 30 °C and at two inlet ozone concentrations (200 and 2000 ppm). At low ozone concentrations (200 ppm) (**Figure.6.a**), α-, β- and γ-MnO_2 exhibited 100% ozone decompositions throughout the analysis of 120 min whereas , the δ-MnO_2 activity is gradually decreased to 92 % in 120 min. These results conforms that at low ozone concentrations the capacity of MnO_2 catalysts for ozone decomposition is very high and it is hard to distinguish their activities. Hence, the inlet ozone concentrations

are increased to tenfold (2000 ppm) to find the optimum activity over all the MnO_2 catalysts. At high ozone concentrations (**Figure.6.b**), the activity of δ-MnO_2 is drastically decreased from 90 to 35 %, whereas the activity over β-MnO_2 is gradually decreased and reached to 70 % after 480 min. On the other hand, α- and γ-MnO_2 exhibited almost 100 % ozone decomposition up to 300 min. Thereafter slight decrease in the activity over α-MnO_2 is noticed. After 480 min, the catalytic activity of α- and γ-MnO_2 are 92 and 100 %, respectively. The change in the ozone decomposition over MnO_2 catalysts might be due to the change in the specific surface area, reducibility, tunnel (phase) structures.

However, the ozone decomposition results are mostly independent to the specific surface area; because, the highest surface δ-MnO_2 (164 m^2/g) shown lowest activity (35 %), whereas lowest surface β-MnO_2 (89 m^2/g) exhibited moderate activity (72 %), which indicates that the specific surface area may not be the exact factor to determine the ozone decomposition. Jia et al., reported that the same as the effect of specific surface area on the ozone decomposition is less significant[26]. On the other hand, Wang et al., reported that the catalysts have high reducibility/under go faster reduction may show high ozone decompositions[10]. From the H_2-TPR results, δ-MnO_2 catalyst reduced at low temperature among all other MnO_2 catalysts, though it is shown lowest activity for ozone decomposition. In case of α-, β- and γ-MnO_2 catalysts also the order of reducibility (α > β > γ) and the order of ozone decomposition (γ > α > β) are not in line with the literature reports[26]. Therefore, the ozone decomposition capacity of MnO_2 catalysts may not concluded with the reducibility results.

MnO_2 tunnel (phase) structure and activity relationship:

As we discussed earlier, the MnO_2 catalysts present the distinct tunnel diameters due to the combination of MnO_6 octahedra in various directions. Among them, δ-MnO_2 presents the layers of edge-sharing MnO_6 octahedra, and the spacing between the two successive edge-sharing MnO_6 octahedra layers is ~7 Å. This diameter is fairly sufficient to the ozone adsorption / diffusion process, but it has shown lowest ozone decomposition, the reason might be due to its larger effective tunnel diameter. Chen et al., observed that the effect of MnO_2 tunnel diameter/size on the HCHO oxidation and reported that the [2 × 2] tunnel structure is much more active than [1 × 1] or [3 × 3] structure since, the effective diameter of the [2 × 2] tunnel is more suitable for the HCHO diffusion[36]. Whereas, the moderate/second lowest activity over β-MnO_2 ascribed to its small tunnel diameter (1.89 Å). Because, β-MnO_2 develops (1 × 1) tunnels by the combination of MnO_6 octahedra through the common corners of the adjacent chains with a diameter of 1.89 Å. This small tunnel diameter may not be favorable for the ozone adsorption/diffusion on the catalyst. This might be the reason for the low activity of β-MnO_2 than α- and γ-MnO_2 catalysts. Similar observations were reported over β-MnO_2 by Jia et al[26].

On the other hand, the high ozone decomposition activities over α- and γ-MnO_2 might be attributed to their effective tunnel diameters (4.6 and 2.3 Å), because these diameter values are close to the ozone molecular diameter (~3 Å). Moreover, the effective tunnel diameter of α-MnO_2 is more accessible than γ-MnO_2. In spite of having smaller effective tunnel diameter, the γ-MnO2 exhibited better ozone decomposition capacity compared to α-MnO_2. This discrepancy in ozone decomposition capacity between γ-MnO_2 and α-MnO_2 can be explained based on the surface properties rather than textural properties.

3.6 Surface atom properties

In order to identify the effected surface atom properties on the decomposition of ozone, all the MnO_2 catalysts are analyzed by XPS analysis and the results are shown in **Figure.7.a**. The Mn $2p_{3/2}$ and Mn $2p_{1/2}$ XPS peaks are centered at about 641.8 and 653.4 eV, respectively. The separation energy between these two peaks of all MnO_2 catalysts is close to 11.6 eV, which is near to that of Mn^{4+} 2p XPS with an octahedral coordination in MnO_2[32,36]. The average oxidation state (AOS) of the MnO_2 catalysts is estimated from Mn 3s spectra by using the following formula: AOS = 8.956 - 1.126 x ΔEs, where ΔEs is the binding energy difference between the doublet Mn 3s peaks and the results shown in **Table.1**[37]. Because, the Mn 3s XPS is more sensitive to the

oxidation state of manganese than that of Mn 2p[36]. From the results (**Figure.8**), the energy differences (E_{3s}) between the main peak and its satellite in the corresponding Mn 3s spectra of α-, β-, γ-, and δ-MnO_2 are 4.57, 4.42, 4.67 and 4.49 eV and their AOS are 3.8, 3.97, 3.69 and 3.9, respectively.

The O 1s XPS spectra of MnO_2 catalysts are shown in **Figure.7.b**. The asymmetrical O 1s spectra could be deconvoluted into two peaks and a peak at 529 eV is assigned to the lattice oxygen (O_2^-) (denoted as O_{latt})[25], and the peak at 531.6 eV corresponds to the surface adsorbed oxygen with low coordination (denoted as O_{ads})[38], such as O_2^{2-} or O^- belong to defect-oxide or hydroxyl-like groups. The surface element molar ratios of O_{ads}/O_{latt} are calculated and summarized in Table 1. From the results, the order of MnO_2 catalysts is γ-MnO_2 (1.84) > α-MnO_2 (1.16) > β-MnO_2 (0.76) > δ-MnO_2 (0.62). The highest O_{ads}/O_{latt} ratio (surface oxygen vacancies) over γ-MnO_2 might be due to the random intergrowth of its crystal structure ((2 x1) and (1 x 1) tunnels) and lowest AOS (3.69). It was reported that, once Mn^{3+} appears in the manganese dioxide, oxygen vacancies will be generated to maintain electrostatic balance according to the following process (e1)[22].

$$4Mn^{4+} + O^{2-} \rightarrow 4Mn^{4+} + 2e^-/V_o + \tfrac{1}{2} O_2 \rightarrow 2Mn^{4+} + 2Mn^{3+} + V_o + \tfrac{1}{2} O_2 \quad \text{(e1)}$$

Where V_o represents an oxygen vacancy site.

The mechanism of ozone decomposition consists mainly two steps: adsorption of ozone on the catalysts and desorption of the adsorbed intermediates[39]. According to the Jia et al., ozone decomposition mechanism over surface oxygen vacancies is following the equations (e2 to e4)[26]:

$$O_3 + V_o \rightarrow O_2 + V_o\text{-}O^{2-} \quad \text{(e2)}$$

$$O_3 + V_o\text{-}O^{2-} \rightarrow O_2 + V_o\text{-}O_2^{2-} \quad \text{(e3)}$$

$$V_o\text{-}O_2^{2-} \rightarrow O_2 + V_o \quad \text{(e4)}$$

This mechanism shows that the ozone decomposition depends up on the density of the oxygen vacancies[40]. From the ozone decomposition results, the activity difference between α- and γ-MnO_2 catalysts might be resulted from the differences between surface oxygen vacancies. Jia et al., reported that the decomposition of ozone over α-, β- and γ-MnO_2 catalysts at low ozone concentrations and noticed highest activity for α-MnO_2 than others, which is ascribed to its lowest average Mn oxidation state and density of oxygen vacancies[26]. In another study, Wang et al., reported ozone decomposition over various OMS-2 (α-MnO_2) catalysts, prepared by varying the Mn metal precursor. The better activity observed over manganese acetate precursor used OMS-2 catalyst, which is also attributed to its lowest Mn average oxidation state and density of oxygen vacancies[10]. Zhao et al., reported NO oxidation over α-, β-, γ- and δ-MnO_2 catalysts and found high catalytic activity over γ-MnO_2, which is ascribed to the large numbers of active oxygen vacancies resulted from the disordered structure of γ-MnO_2[32]. From these reported results it can be conclude that the oxygen vacancies are playing the major role besides the tunnel diameter.

The observed ozone decomposition results are in consistent with the reported data, which states that the catalysts have high oxygen vacancies shown higher activity than others. From the XPS data, the surface oxygen vacancies of γ-MnO_2 (1.8) are higher than that of α-MnO_2 (1.6). This high surface oxygen vacancies offered high ozone decomposition to the γ-MnO_2 than that of α-MnO_2. The formation of high surface oxygen vacancies over γ-MnO_2 might be due to its disordered tunnel structure with abundant stacking faults and facile preparation method[32]. On the other hand, the surface abundant Mn^{3+} (AOS) on MnO_2 catalysts may also favor the ozone decomposition by changing the redox cycle between Mn^{3+} and Mn^{4+}. Liu et al. observed a linear correlation between ozone decomposition and Mn^{3+} content on AgMn/HZSM-5[41]. Wang et al., also reported the same as ozone initially reacts with Mn^{3+} and forms the [$Mn^{4+}O^-$] complex on OMS-2 catalyst, later this complex reacts with another ozone molecule and reproduce to the Mn^{3+} state by eluting two O_2 molecules[10]. Therefore, the amount of Mn^{3+} on the surface also contributes the ozone decomposition. If we look at the Mn AOS of α- and γ-MnO_2 catalysts, the AOS of γ-MnO_2 is lower (high Mn^{3+}) than α-MnO_2. This is also a one of the major reason along with oxygen vacancies for high ozone decomposition capacity of γ-MnO_2 than that of α-MnO_2. The lower activity of β-MnO_2 and δ-MnO_2 also supported by XPS results along

with tunnel structure, by showing lower surface oxygen vacancies (0.76 and 0.62) and higher AOS of Mn (3.97 and 3.9) than the α-MnO_2 and γ-MnO_2 catalysts.
Overall, the results combined with the above structural analysis suggest that the random tunnel structure of γ-MnO_2 with abundant stacking faults is the main source for the high surface oxygen vacancies and Mn^{3+} amount than the other three phases, which efficiently accelerated ozone decomposition.

4. CONCLUSION

In summary, α-, β-, γ- and δ-type MnO_2 catalysts are prepared and observed their very different activities for the catalytic decomposition of ozone. The significant differences in activities over various MnO_2 phases are ascribed to their different physical properties, tunnel structures, AOS of Mn, and surface oxygen vacancies. However, the tunnel structures, surface oxygen vacancies and AOS of Mn might played a major role in the ozone decomposition reaction. The random tunnel structure of γ-MnO_2 has provided most active surface oxygen vacancies and the lowest AOS of Mn on the catalyst surface. Therefore, the γ-MnO_2 catalyst presented the highest ozone decomposition capacity among the other types of MnO_2 catalysts. Due to the high catalytic ozone decomposition capacity, γ-MnO_2 may potentially be used as a catalyst in the purification of ozone contain waste gases as well as in the application of ozone assisted catalytic oxidation of volatile organic compounds.

Acknowledgements
The author(s) received no financial support for the research, authorship, and/or publication of this article.

Conflict of Interest
The author(s) do not have any conflict of interest.

REFERENCES:

[1] Penko, N.; Krassimir, G.; Petya, K.; Katya, M.; Todor, B.;Vladimir, G.; Narendra, K.; K.Sarker, D.; Dimitar, P.; Slavcho, R. *J. Haz. Mat.* **2010,** *184*, 16-19
[2] Rakitskaya, T.L.; Bandurko, A.Yu.; Ennan, A.A.; Paina, V.Ya.; Rakitskiy, A.S. *Microporous Mesoporous Mater.* **2001,** *43(2),*153-160
[3] Kumar, N.; Konova, P.; Naydenov, A.; Salmi, T.; Murzin, D.Y.; Heikillä, T.; Lehto, V.P. *Catal. Today*. **2007**, *119*, 342-346.
[4] Lian, Z.; Ma, J.; He, H. *Catal. Commun.* **2015**, *59*, 156-160
[5] Dhandapani, B.; Oyama, S.T.; *Appl. Catal. B Environ.* **1997**, *11*, 129-166
[6] Kwong, C.W.; Chao, C.Y.H.; Hui, K.S.; Wan, M.P. *Environ. Sci. Technol.* **2008**, *42,* 8504-8509
[7] Yu, Y.; Wang, H.; Li, H.; Tao, P.; Sun, T. *Chemosphere***.** **2022**, *298*, 134187
[8] Ye, L.; Dai, W.; Lu, P.; Huang, J.; Yan, X.; Sun, C.; He, K.; Zhang, M.; Huang, H. *Applied Catalysis B: Environment and Energy***.** **2024**, *345*, 123696
[9] Batakliev, T.; Tyuliev, G.; Georgiev, V.; Anachkov, M.; Eliyas, A.; Rakovsky, S. *Ozone: Sci. Eng.* **2015**, *37*, 216-220
[10] Wang, C.; Ma, J.; Liu, F.; He, H.; Zhang, R. *J. Phys. Chem.C.* **2015**,*119*, 23119
[11] Zhang, B.; Ji, J.; Liu, B.; Zhang, D.; Liu, S.; Huang, H. *Applied Catalysis B: Environmental*. **2022,** *315*, 121552
[12] Wang, Z.; Li, T.; Zhang, S.; Zhang, R.; Zhang, Y.; Zhong, Q. *Chemical Engineering Journal***.** **2024**, *488*, 150693
[13] Yang, H.H.; Du, J.; Wu, M.; Zhou, H.; Yi, X.; Zhan, J.; Liu, Y. *Chemical Engineering Journal.* **2022,** *427,* 132075
[14] Liu, B.; Yi, Z.; Yang, Y.; Li, Y.; Yang, J.; Zhu, M. *App. Cata. B: Envi.* **2023,** *334,* 122788
[15] Wang, H.C.; Liang, H.S.; Chang, M.B. *J. Hazard. Mater.* **2011**,*186*, 1781
[16] Yang, Y.; Li, J.; Xiao, Z.; Yun, Y.; Zhu, M.; Yang, J. *Chemosphere***.** **2024,** *358*, 142113
[17] Ma, J.; Wang, C.; He, H. *App. Cat. B: Envi.* **2017,** *201,* 503-510,
[18] W. Tang, H. Liu, X. Wu, Y. Chen, Ozone Sci. Eng. 36 (2014) 502.
[19] B. Bai, J. Li, J. Hao, Appl. Catal. B Environ. 164 (2015) 241.
[20] Zhang, L.; Wang, S.; Lv, L.; Ding, Ya.; Tian, D.; Wang, S. *Langmuir.* **2021**, *37*(4), 1410–1419
[21] Wei, C.; Yu, L.; Cui, C.; Lin, J.; Wei, C.; Mathews, N.; Huo, F.; Sritharan, T.; Xu, Z. *Chem. Commun. (Camb).* **2014**, *50*, 7885
[22] Wang, F.; Dai, H.; Deng, J.; Bai, G.; Ji, K.; Liu, Y. *Environ. Sci. Technol.* **2012**, *46*, 4034
[23] Lu, J-l.; Wang, S.; Zhao, K.; Wang, T.; Ni, C-j.; Wang, M-z.; Wang, S-d. *J. of Fuel Che. and Tech.* **2021,** *49 (7)*, 1014-1022
[24] Liang, S.H.; Bulgan, F.T.G.; Zong, R.L.; Zhu, Y.F. *J. Phys. Chem. C.* **2008**, *112*, 5307

[25] Si, W.; Wang, Y.; Peng, Y.; Li, X.; Li, K.; Li, J. *Chem. Commun.* **2015**, *51*, 14977
[26] Jia, J.; Zhang, P.; Chen, L. *Appl. Catal. B Environ.* **2016**, *189*, 210
[27] Devaraj, S.; Munichandraiah, N. *J. Phys. Chem. C.* **2008**,*112*, 4406
[28] Zhang, J.; Li, Y.; Wang, L.; Zhang, C.; He, H. *Catal. Sci. Technol.* **2015**, *5*, 2305
[29] Wang, X.; Li, Y. *Chemistry*. **2003**, *9*, 300
[30] Gao, T.; Fjellvåg, H.; Norby, P. *Anal. Chim. Acta*. **2009**, *648*, 235
[31] de Wolff, P.M. *Acta Crystallogr.* **1959**, *12*, 341
[32] Zhao, B.; Ran, R.; Wu, X.; Weng, D. *Appl. Catal. A Gen.* **2016**, *514*, 24
[33] Wang,Y.; Indrawirawan, S.; Duan, X.; Sun, H.; Ang, H.M.; Tadé, M.O.; Wang, S. *Chem. Eng. J.* **2015**, *266*, 12
[34] Benhaddad, L.; Makhloufi, L.; Messaoudi, B.; Rahmouni, K.; Takenouti, H. *J. Mater. Sci. Technol.* **2011**, *27*, 585
[35] Li, Y.; Fan, Z.; Shi, J.; Liu, Z.; Shangguan, W. *Chem. Eng. J.* **2014**, *241*, 251
[36] Chen, T.; Dou, H.; Li, X.; Tang, X.; Li, J.; Hao, J. *Microporous Mesoporous Mater.* **2009**, *122*, 270
[37] Yang, Y.; Huang, J.; Wang, S.; Deng, S.; Wang, B.; Yu, G. *Appl. Catal. B Environ.* **2013**, *568*, 142-143
[38] Hou, J.; Li, Y.; Liu, L.; Ren, L.; Zhao, X. *J. Mater. Chem. A.* **2013,** 1, 6736
[39] Li, W.; Gibbs, G. V.; Oyama, S.T. *J. Am. Chem. Soc.* **1998**, *120*, 9041
[40] López, J.M.; Gilbank, A.L.; García, T.; Solsona, B.; Agouram, S.; Torrente-Murciano, L. *Appl. Catal. B Environ.* **2015,** *403*, 174-175
[41] Liu, Y.; Li, X.; Liu, J.; Shi, C.; Zhu, A. *Chinese J. Catal.* **2014**, *35*, 1465

Table.1: Tunnel properties, XPS data, specific surface area (m^2/g), Pore volume (cm^3/g) and H_2 consumption (mmol/g) of α-, β-, γ- and δ-MnO_2 catalysts.

Catalyst	Tunnel	Size/Å	XPS Data		specific surface area (m^2/g)	Pore volume (cm^3/g)	H_2 consumption (mmol/g)
			Mn 3s	O 1s			
			AOS	O_{ads}/O_{latt}			
α-MnO_2	(1 x 1), (2 x 2)	1.89, 4.60	3.80	1.16	159	0.36	11.25
β-MnO_2	(1 x 1)	1.89	3.97	0.76	89	0.24	13.10
γ-MnO_2	(1 x 1), (1 x 2)	1.89, 2.30	3.69	1.84	119	0.33	12.20
δ-MnO_2	interlayer	7.00	3.90	0.62	164	0.42	10.25

Figure Captions:
Figure.1: XRD patterns of α-, β-, γ- and δ-MnO_2 catalysts
Figure.2: crystal structures of α-, β-, γ- and δ-MnO_2 phases
Figure.3: SEM images of α-, β-, γ- and δ-MnO_2 catalysts, 1 and 2 refer to different magnifications of one sample.
Figure.4: Nitrogen adsorption/desorption isotherms and BJH pore size distributions (inset) of α-, β-, γ- and δ-MnO_2 catalysts
Figure.5: H_2-TPR profiles of α-, β-, γ- and δ-MnO_2 catalysts
Figure.6: ozone conversion Vs time of α-, β-, γ- and δ-MnO_2 catalysts at an inlet ozone concentrations of a) 200 ppm and b) 2000 ppm. GHSV=600000 mL/g.h
Figure.7: Mn 2p and O 1s XPS spectra of α-, β-, γ- and δ-MnO_2 catalysts.
Figure.8: Mn 3s XPS spectra of α-, β-, γ- and δ-MnO_2 catalysts

International Journal of Environmental Sciences
ISSN: 2229-7359
Vol. 11 No. 10s, 2025
https://www.theaspd.com/ijes.php

Figure.1

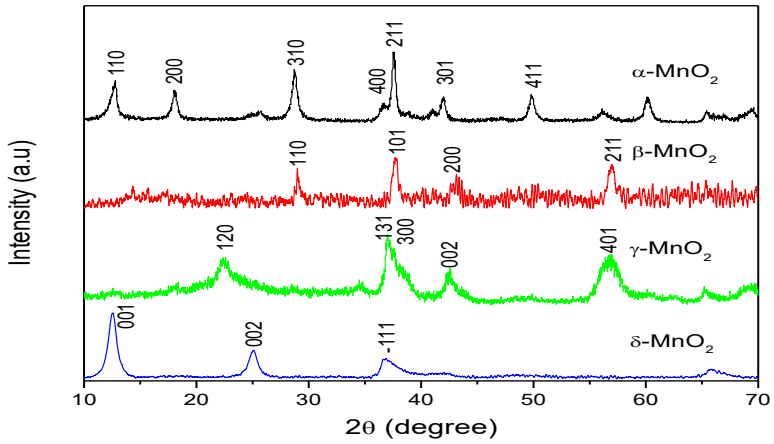

Figure.2

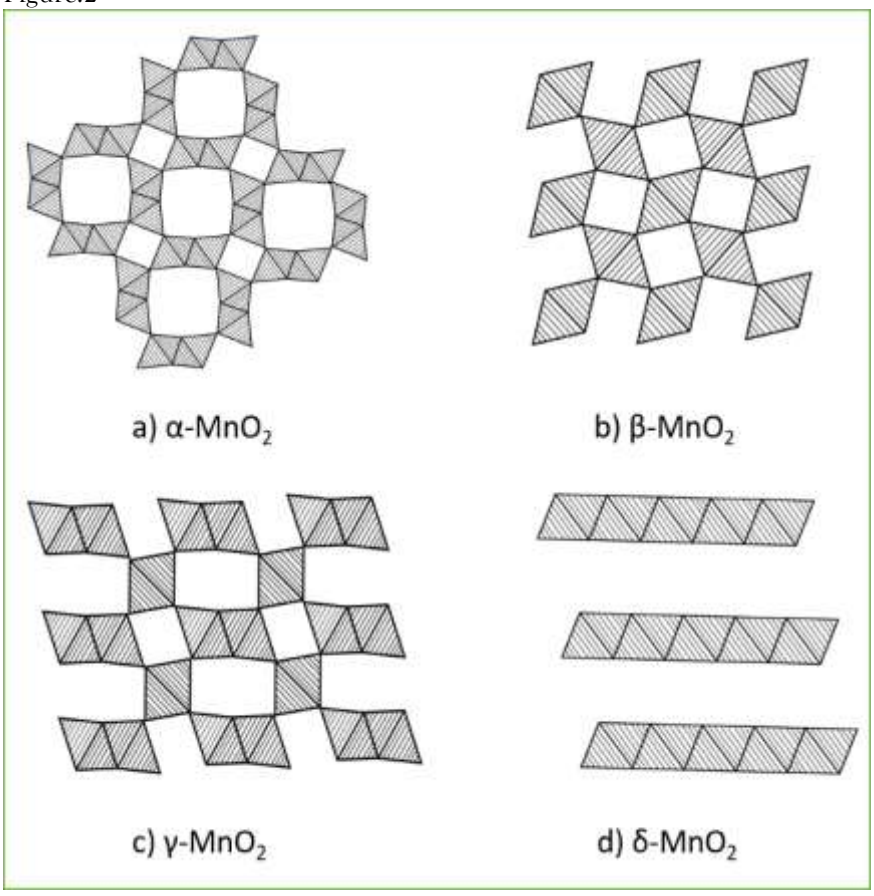

Figure.3

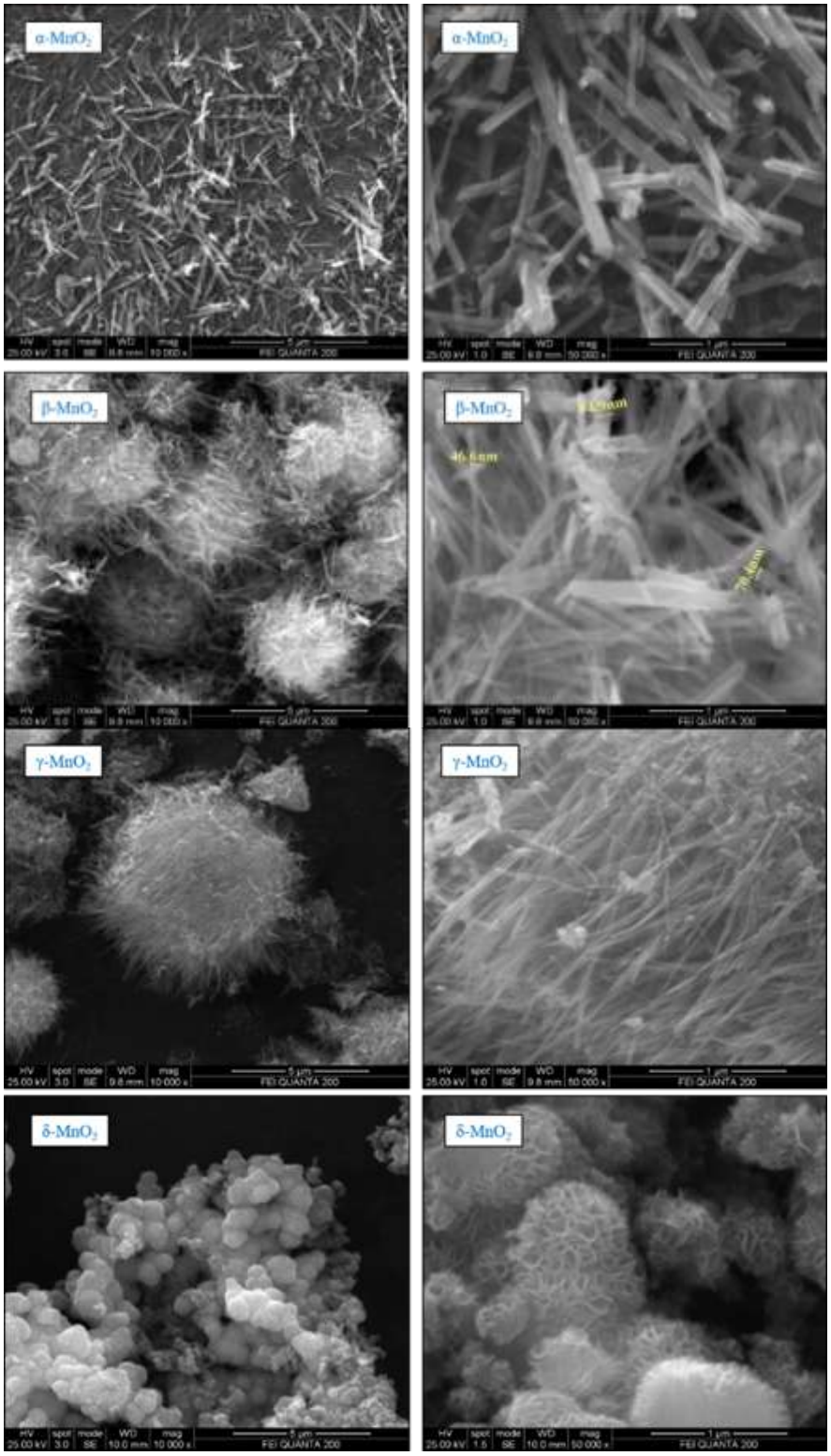

Figure.4

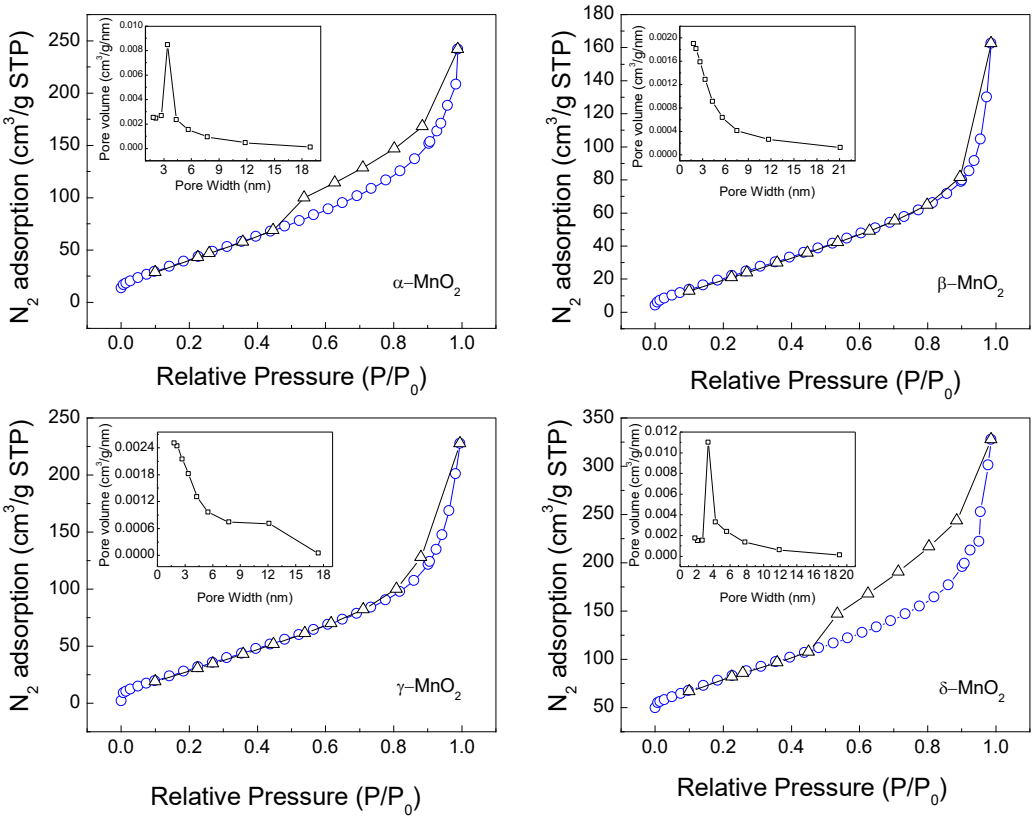

Figure.5

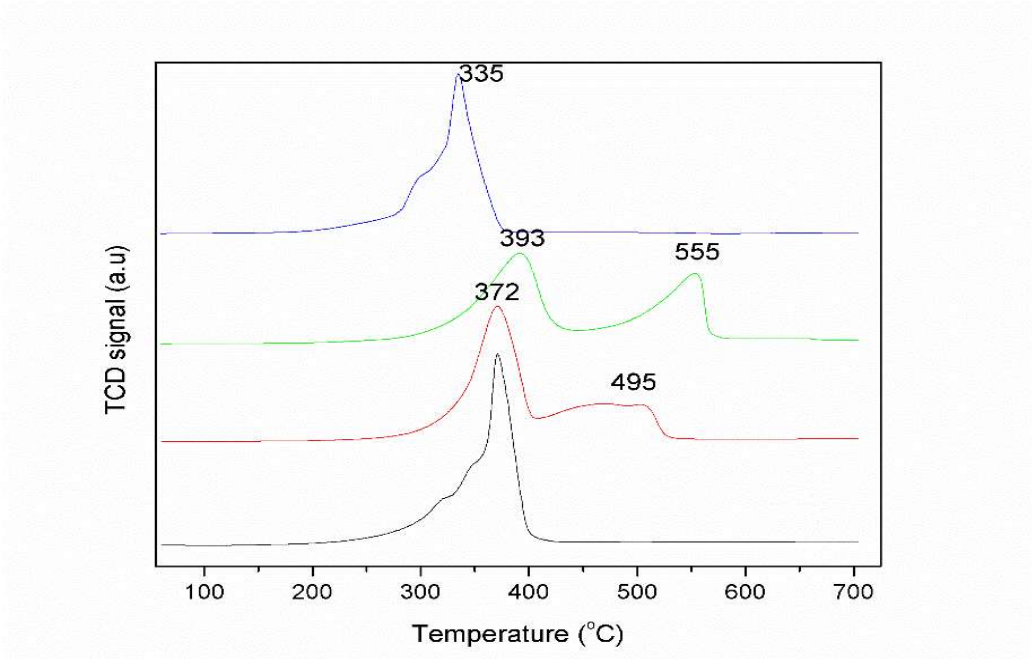

Figure.6

International Journal of Environmental Sciences
ISSN: 2229-7359
Vol. 11 No. 10s, 2025
https://www.theaspd.com/ijes.php

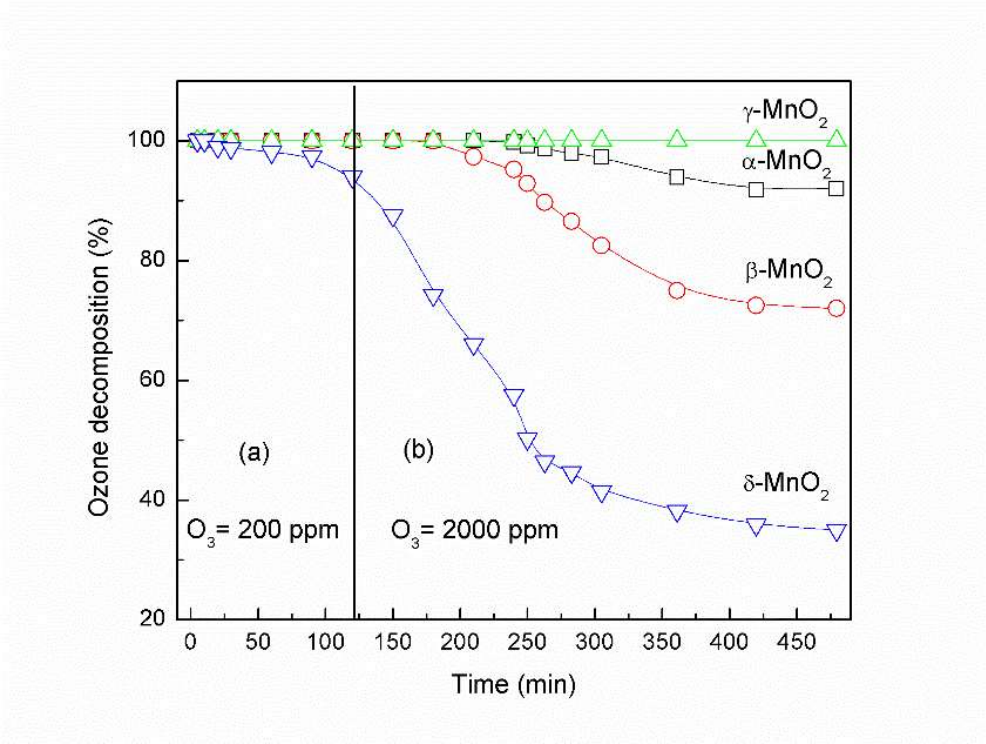

Figure.7

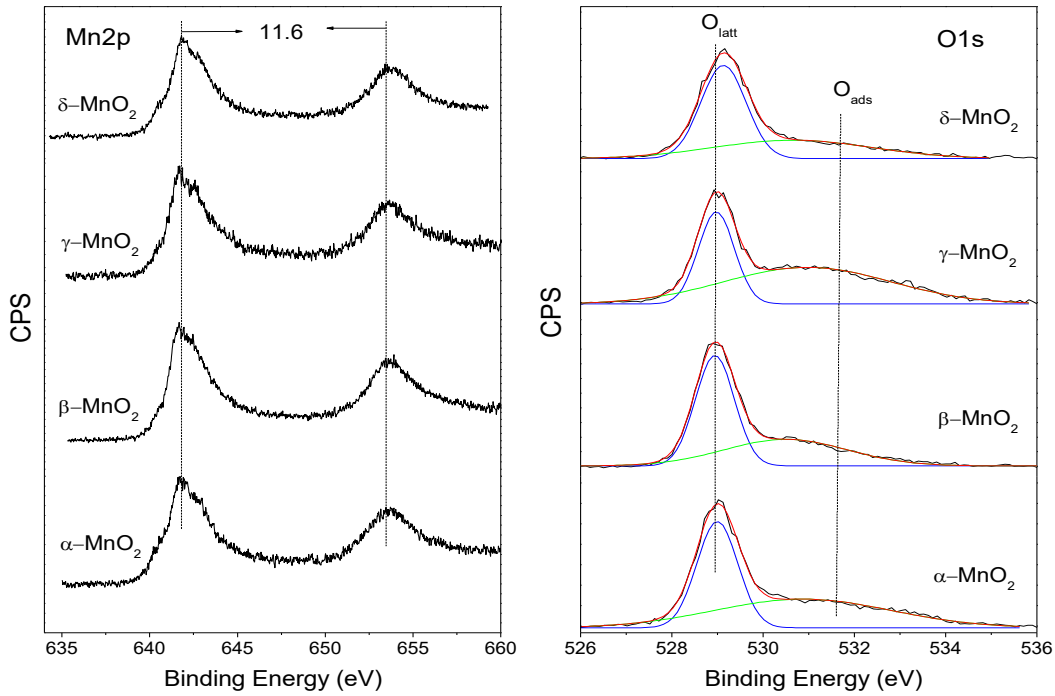

Figure.8

International Journal of Environmental Sciences
ISSN: 2229-7359
Vol. 11 No. 10s, 2025
https://www.theaspd.com/ijes.php